

Article

The Role of the Synthesis Routes on the CO-Sensing Mechanism of NiO-Based Gas Sensors

Adelina Stanoiu¹, Corneliu Ghica¹ , Catalina Gabriela Mihalcea^{1,2}, Daniela Ghica¹ 
and Cristian Eugen Simion^{1,*} 

¹ National Institute of Materials Physics, Atomistilor 405A, 077125 Magurele, Romania

² Faculty of Physics, University of Bucharest, Atomistilor 405, 077125 Magurele, Romania

* Correspondence: simion@infim.ro; Tel.: +40-21-24118134

Abstract: In this study, two alternative synthesis routes have been used in obtaining gas-sensitive NiO materials. The structural and morphological aspects were systematically investigated by X-ray diffraction (XRD) and transmission electron microscopy (TEM), revealing significant differences further mirrored in their sensing performances. Simultaneous electrical resistance and contact potential differences have been involved aiming to decouple the energetic contributions: work function ($\Delta\Phi$), surface band bending ($q\Delta V_s$) and electron affinity ($\Delta\chi$). Two sensing mechanism scenarios explained the enhancement and downgrading in the sensor response to carbon monoxide (CO) concerning the synthesis strategies. The role of relative humidity (RH) was considered throughout the electrical operando (in-field) investigations.

Keywords: nickel oxide sensitive material; simultaneous electrical resistance and contact potential differences; carbon monoxide sensing mechanism



Citation: Stanoiu, A.; Ghica, C.; Mihalcea, C.G.; Ghica, D.; Simion, C.E. The Role of the Synthesis Routes on the CO-Sensing Mechanism of NiO-Based Gas Sensors. *Chemosensors* **2022**, *10*, 466. <https://doi.org/10.3390/chemosensors10110466>

Academic Editors: Xiaoxing Zhang and Hao Cui

Received: 20 October 2022

Accepted: 6 November 2022

Published: 9 November 2022

Publisher's Note: MDPI stays neutral with regard to jurisdictional claims in published maps and institutional affiliations.



Copyright: © 2022 by the authors. Licensee MDPI, Basel, Switzerland. This article is an open access article distributed under the terms and conditions of the Creative Commons Attribution (CC BY) license (<https://creativecommons.org/licenses/by/4.0/>).

1. Introduction

Early in the 1950s, two American scientists, Brattain and Bardeen, discovered that the conductivity of a metal oxide semiconductor (MOX) changes when gas adsorption takes place on the surface of the sensitive material [1]. After ten years, Taguchi brought into the market the first gas sensor based on SnO₂ [2]. Since that moment, academic and industrial workers have started to improve the know-how/applicative level related to the gas sensors when operated under real-life conditions (e.g., presence of variable relative humidity-RH, interfering gases, constant atmospheric pressure). Several issues keep the research in a continuous ongoing process. These arouse quantifiable facts such as best sensitivity, high selectivity, optimum stability in time, fast response and recovery transients, low power consumption and less impact of the relative humidity over the previously mentioned gas sensing performances [3]. However, despite the relatively simple gas detection working principle, the gas sensing mechanisms of MOX are quite complex [4]. Generally accepted, it is based on oxidation/reduction surface reactions followed by the subsequent electronic/ionic involvement behaviour. Therefore, one must have a realistic view at the “microscopic” level of the type and role of different gas species involved in the surface reactions and the way in which the associated electronic changes are addressed [5].

Nickel oxide (NiO) with Ni singly or doubly charged vacancies behaves as a p-type MOX material, less studied for its sensing potential [6]. Nevertheless, the oxide cannot form double bonds with oxygen, thus leaving Ni vacancies available as active sites in the catalytic conversion of hydrocarbons to CO₂ and H₂O [7]. To preserve overall electrical neutrality in the crystal, two Ni²⁺ ions should be converted to Ni³⁺ for every vacant Ni²⁺ site [8]. The Ni³⁺ ions introduced within the crystal in this way can be advised to be positive and centre-stable of jumping from one Ni site to another. When an electron hops from a Ni²⁺ to a Ni³⁺ site, it is as if a positive hole moves around the Ni²⁺ sites.

The working principle of a common p-type MOX material is based on the modulation of the energy barrier heights at the grain-to-grain interface where an accumulation layer of holes is formed [9]. Moreover, the overall gas-sensing process takes place on various reaction sites, thus relating its performance to morphological aspects (e.g., shape and size). Accordingly, sensitive NiO with decreased particle size and increased specific surface area, resulting in a high surface-to-volume ratio, are recommended for gas sensing detection. As was demonstrated by Barsan et al. [10] in the case of p-type materials the sensor response depends on both grain and grain-to-grain contact size, since the surface-hole flow is highly influenced by such aspects and less by the atomic faces exposed to the target gases [11].

Moreover, in the field of gas sensing, it has always been a challenge to enhance the sensitivity and selectivity of the sensors when operated under real-life conditions. Herein, the NiO-based gas sensors exhibit a low influence from the presence of RH on their sensing performances [12]. With all these, the interest for NiO as a based gas-sensitive material is rather low due to its lack of sensitivity when compared to n-type MOX materials. Spanning the literature, we found that NiO deposited via DC sputtering exhibits a good selectivity towards formaldehyde detection when operated at 200 °C without considering the role of humidity [13]. Mokoena et al. [14] revealed good sensitivity and fast transients to n-propanol detection in dry and humid backgrounds operated at 75 °C. Qian et al. fabricated hierarchical flake-flower NiO by using a hydrothermal method. They showed good selectivity to 5 ppm of carbon monoxide (CO) with a sensor response factor of 20 at the optimal operating temperature of 250 °C. A sensing mechanism was presented without considering the role of RH [15].

Herein, we focus on operando investigations of simultaneous electrical resistance and contact potential difference to highlight the role induced by different synthesis routes upon the gas sensing mechanism towards CO detection.

2. Materials and Methods

2.1. Powders Synthesis and Sensors Fabrication

The first NiO hydrothermal synthesis route was extensively described elsewhere [16]. Briefly, Ni(NO₃)₂ was dissolved in distilled water and mixed with ethylene-diaminetetraacetic acid (EDTA) for complexing. Ethylene glycol (EG) was used as a template. The precipitate obtained after hydrothermal treatment at 180 °C for 24 h was filtered and washed with water and ethanol, dried, and thermally treated in the air at 400 °C for 8 h.

The second synthesis route was performed by a solvothermal synthesis method templated by Tripropilamina (TPA). Ni acetylacetonate (Ni (Ni(C₅H₇O₂)₂)), dissolved in ethanol, was used as an inorganic precursor. The polyvinylpyrrolidone (PVP) dispersed in ethanol under strong stirring conditions was added as a stabilizing agent. The pH was adjusted to 11-value Tetrabutylammonium-hydroxide solution, 40 wt.% (TBAOH). The solvothermal-treated solution at 180 °C for 24 h was kept at room temperature for several days for gelation. The obtained gel was dried under vacuum at 80 °C and thermally treated at 400 °C for 8 h in air.

The as-prepared powders were ground to remove agglomerates and then mixed with α -terpinol to obtain a proper consistency of the paste. Subsequently, the paste was deposited over the commercial alumina (Al₂O₃) substrates provided with Pt interdigital electrodes on top and Pt heater on the back side, by the screen-printing technique. The sensors are having the following dimensions: 25 mm length; 4 mm width; 0.7 mm thickness. The interdigital distance between the Pt electrodes and the Pt thickness is 200 μ m and 5 μ m, respectively. The sensitive layer thickness is about 50 μ m. A final heating process removes the organic solvent and ensures a good adherence of the NiO layers to the substrates. The obtained sensors have been labelled as: NiO1 400 and NiO2 400 with respect to the differences induced by the synthesis strategies. The Pt heater (on the Al₂O₃ backside) was calibrated to further set the temperature layer during sensing evaluation.

2.2. Materials Characterization

2.2.1. Morpho-Structural Investigations

X-ray diffraction (XRD) measurements were performed using a Bruker D8 Advance X-ray diffractometer in Bragg-Brentano configuration, with a Cu anode and Ni filter ($\lambda = 0.154184$ nm). TOPAS v.3 was used for Rietveld structural analysis of the XRD patterns. The morphology and structure of the NiO powders were investigated using a JEOL-JEM 2100 transmission electron microscope. The NiO powder was mixed with ethanol, and then small droplets of liquid containing nanoparticles were drop-casted on the lacey carbon membrane of the TEM (transmission electron microscopy) grids.

2.2.2. Gas-Sensing Investigations

The NiO sensors have been characterized for their gas sensing performances by DC electrical investigation in a dynamic gas-flow regime ensured by using a fully computerized Gas Mixing Station (GMS). The phenomenological investigations involved simultaneous electrical resistance (R) and contact potential differences (CPD) accomplished by connecting the McAllister Kelvin Probe to the GMS (Figure 1).

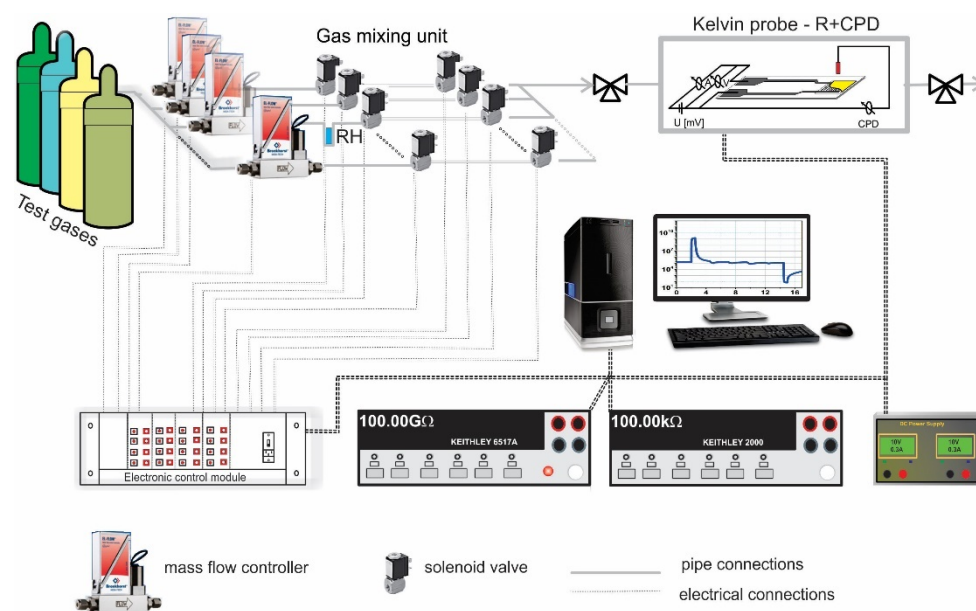


Figure 1. Schematic picture of the Gas Mixing Station used during the gas sensing investigations.

The GMS is operated by dedicated software programmed using Agilent VEE-Pro. The mass flow controllers and the solenoid valves are controlled via Digital/Analog cards. An Analog/Digital card is used to check the performance of the gas mixing station by recording the actual gas flows through the mass flow controllers. The gas channels consist of high-grade Teflon (PTFE) pipes to avoid possible gas contaminations. High-grade test gases are used, their concentrations being adjusted by controlling the ratio of test gas flow to the total gas flow. During all of the processes of gas-sensing characterization, the total flow rate through the system was kept constant at 200 mL/min. The relative humidity changes are attained by passing the carrier gas (synthetic air 5.0) through a vaporizer filled with an adsorbent with a highly specific surface (Chromosorb P-NAW Macherey-Nagel) and kept at room temperature.

The first gas-testing protocol was used to identify the optimum operating temperature for CO detection. The second step was to use this temperature to obtain the sensor response, for different CO concentrations (in the range 10–100 ppm) and variable RH (10–50%). The last type of phenomenological investigation was oriented toward the CO-sensing mechanism.

3. Results

3.1. Structural and Morphological Results

The XRD patterns of both samples have been indexed as face-centred cubic (fcc) NiO, space group Fm-3m (225), ICDD—01-071-1179 (Figure 2).

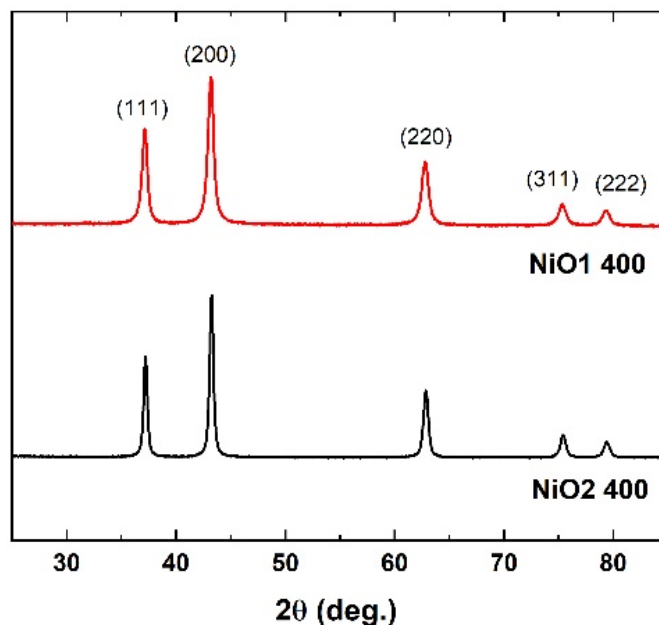


Figure 2. XRD patterns of the NiO samples, indexed with the fcc structure according to ICDD—01-071-1179.

Broader XRD peaks are observed for NiO1 400 with respect to the peaks of NiO2 400, suggesting a lower crystallinity degree of the corresponding nanoparticles. Indeed, the Rietveld analysis determined the volume averaged crystallite size $d = 11 \pm 2$ nm for NiO1 400 and $d = 19 \pm 2$ nm for NiO2 400. The same lattice parameter $a = 0.4178 \pm 0.0001$ nm was calculated for both samples.

The micro-structure and morphology of the two samples have been analyzed using transmission electron microscopy and the results are shown in Figure 3.

The diffraction patterns indicate the fcc structure for both samples, with the most intense diffraction rings corresponding to (111), (200) and (220) crystallographic planes (see insets of Figure 3a,b). The TEM images in Figure 3a,b reveal the differences regarding the morphology of the investigated samples. The NiO1 400 sample shows a porous structure, consisting of self-assembled nanoparticles with an average size of 9 nm. The nanoparticles are not closely packed, allowing the presence of large pores with sizes even larger than the nanoparticles dimensions (see Figure 3a,c). The mean size (diameter) of the NiO1 400 nanoparticles corresponds into the error limit to the crystallite size determined by XRD. On the other hand, the NiO2 400 sample is made of larger quasi-spherical nanoparticles (mean size of 29 nm) with a tendency of faceting (Figure 3b,d). Compared with NiO1 400, the NiO2 400 sample is more compact as the constituent nanoparticles are closely packed. However, the quasi-spherical morphology of the NiO2 400 nanoparticles results in a quantitatively lower contact surface (interface) at the particle agglomeration, than in the case of the self-assembled nanoparticles of NiO1 400. Moreover, the mean size (diameter) of the NiO2 400 nanoparticles is larger than the crystallite size determined by XRD, indicating the presence of at least two coherent structural domains (crystallites) in many nanoparticles (see a detailed comment in Ref. [17]). The broad particle size distribution with a standard deviation of 10 nm (Figure 3d) supports the same conclusion. Such intrinsic parameters are mirrored within the gas-sensing performances, namely, through the different gas interaction mechanisms [18]. These are strongly related to the surface crystallographic structure in the form of nickel vacancies [19]. In this respect, it is reasonable to assume that the fingerprint

of a higher surface reactivity is given by the number of surface defects. Since the NiO2 400 has a tendency towards faceting, this will be one of the main aspects in lowering the sensor signal [20]. An explanation of the faceting of NiO grains can be given if one takes into account that the calcination temperature used was sufficiently high enough in such a way that the atoms will be redistributed in order to decrease the total system energy [21].

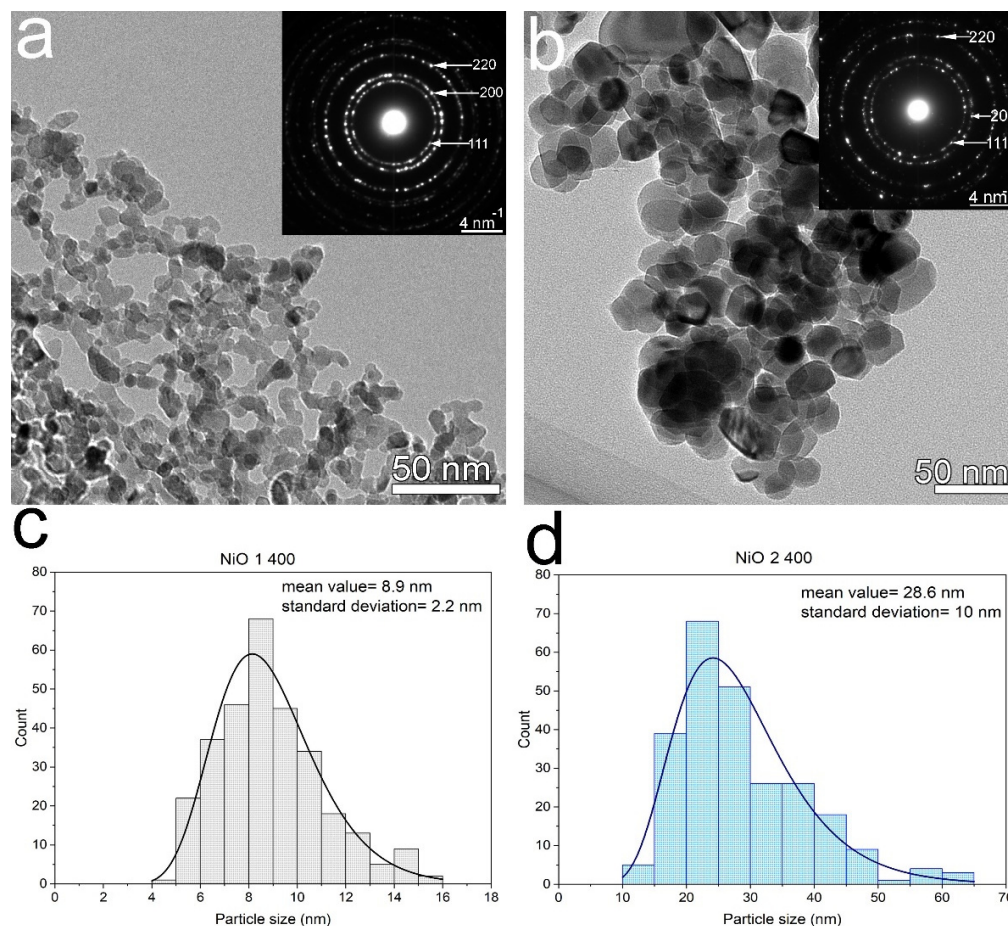


Figure 3. TEM images and corresponding SAED patterns (inset) of (a) NiO1 400 and (b) NiO2 400, and the size histograms obtained after measuring 250–300 nanoparticles from low-magnification TEM images along with the log-normal fitting for (c) NiO1 400 and (d) NiO2 400.

3.2. Gas Sensing—Electrical and Phenomenological Results

According to the mechanism proposed by Springhorn et al. [22], electrical conduction occurs by charge hopping between metal cations (Ni^{2+}) from the same element, with different oxidation states located in the same lattice [23]. Knowing that the operating temperature strongly affects the gas-sensing performances of MOX based gas sensors, in Figure 4 one can see the typical bell-like shape response of both sensors towards 50 ppm of CO exposure under 50% RH. The sensor response was calculated according to Equation (1).

$$S = R_{\text{CO}}/R_{\text{air}} \quad (1)$$

where R_{CO} is the electrical resistance under 50 ppm CO exposure and R_{air} is the electrical resistance under reference synthetic air with 50% RH.

The differences within the responses might be a consequence of the coarser microstructure obtained using different chemistry approaches and of the relationships with the oxygen and water species interplay at the surface [24].

It is well known that the presence of moisture in the target gas atmosphere, affects the overall sensing performances of MOX-based gas sensors. The main reason is related to

the fact that the dissociated hydrogen ions (H^+) and hydroxyl groups (OH^-) compete for the same active sites with the target gas molecules [25]. Therefore, to evaluate the sensor response of NiO-based gas sensors, we undertook the electrical resistance measurements at different relative humidity levels (10%, 30% and 50%) and wide range of CO concentrations (10–100 ppm) at the optimum operating temperature of 250 °C (Figure 5).

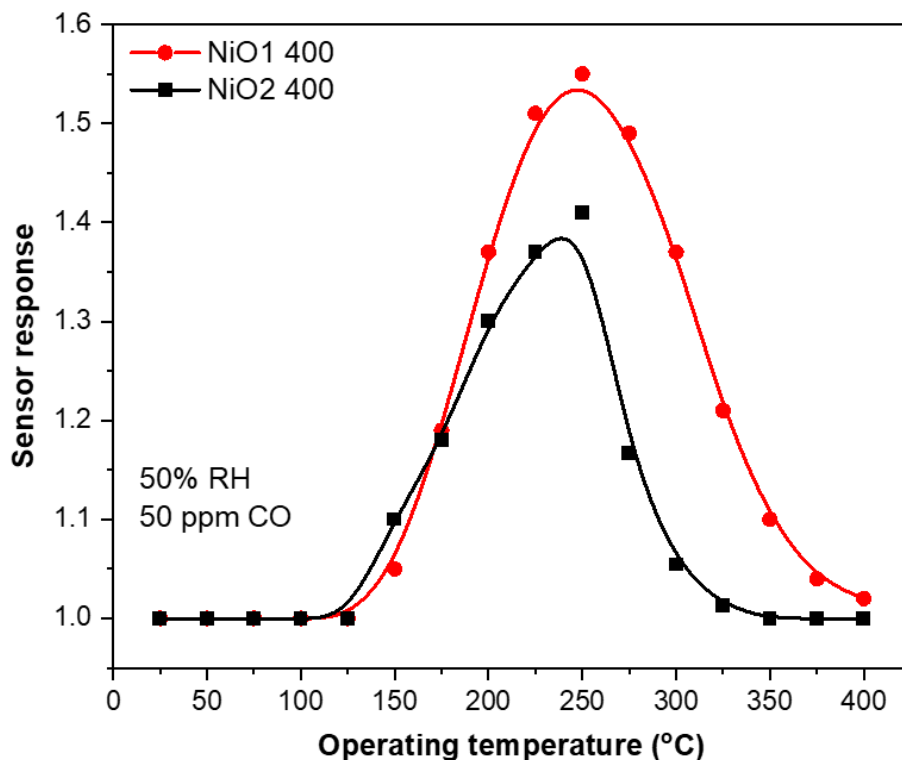


Figure 4. Sensor response of NiO1 400 and NiO2 400 to 50 ppm CO in the presence of 50% RH.

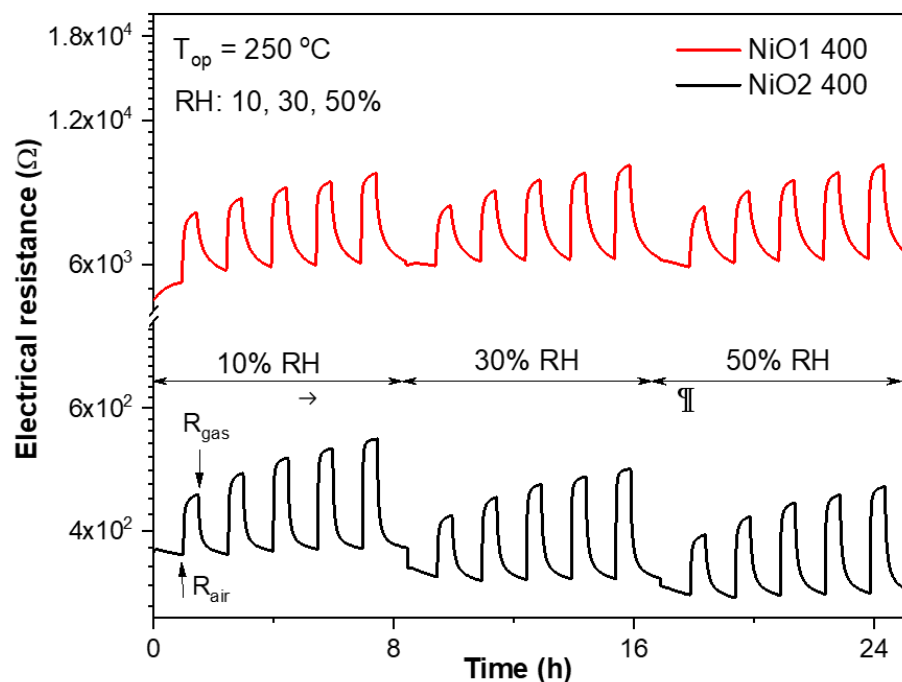


Figure 5. Electrical resistance behaviour for NiO1 400 and NiO2 400 when operated at 250 °C and exposed to 10–100 ppm of CO over 10–50% RH.

The effect of RH upon both baseline resistance (R_{air} in Figure 5) and sensor response (Figure 6) are worth discussing. Thus, from the point of view of the baseline electrical resistance, one can see that NiO1 400 revealed a humidity-tolerant behaviour, the R_{air} variation at the %RH change being negligible. For NiO2 400, the easily noticeable decrease in the baseline resistance is 10% for 30%RH and 15% for 50%RH under similar operating conditions.

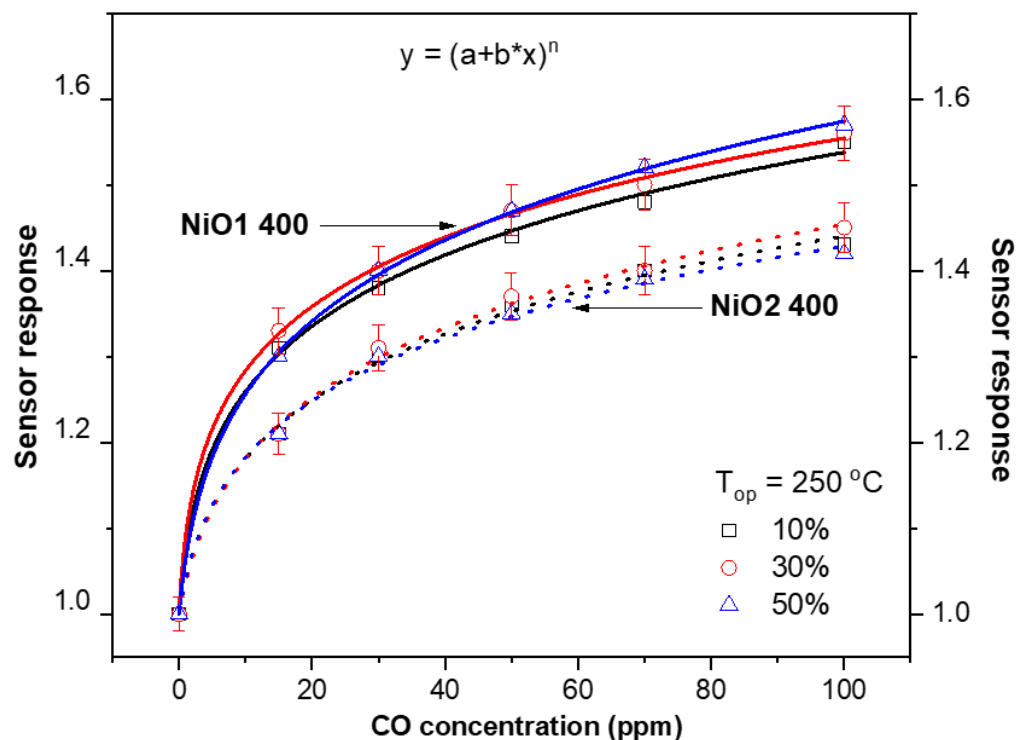


Figure 6. Sensor response for NiO1 400 and NiO2 400 when operated at 250 °C and exposed to 10–100 ppm of CO with 10–50% RH in the background atmosphere.

Related to the sensor response (Figure 6), the dependencies were nicely fitted with the power law function, revealing that NiO1 400 exhibited a 9% higher response than NiO2. Clifford and Tuma have carried out a comprehensive investigation [26] related to the power-law response of basic semiconductor gas sensors. Thus, mass-action law and charge transfer mode were applied to the gas–surface interaction processes. In this respect, the power law exponent strongly depends on the charge state of the surface adsorbed species and surface reaction involving different oxygen species. The specific gas–surface interaction mechanisms exhibit different exponent factor of the power law sensor response reaction [27]. In our case, NiO1 400 nanoparticles have an average size of 9 nm, much smaller than 28.6 nm in the case of NiO2 400. In other words, the smaller the grain sizes (more chemically surface reactive sites), the greater the sensor response.

3.3. Gas Sensing Mechanism Involved in CO Detection

It is generally accepted that the p-type conductivity of NiO material consists of metallic cation deficiency (Ni_{1-x}O) based on nickel vacancies (V_{Ni}). The as-created Ni ions behave as electron acceptors (donating holes) affecting the general conductivity of the material. According to the XPS investigations performed on NiO [28], the binding energies for Ni^{2+} are: 854.5, 856.0, 861.5, 873.0 and 879.8 eV. Moreover, Sawatzky et al. [29] have identified that at the edge of the valence band $\text{Ni}3d^8$ orbital is formed, whereas $\text{O}2p^6$ is just below the Ni band, forming a mixture of these two. However, based on the literature references [30], it can be assumed that the formation of lattice oxygen vacancies under an oxygen-full atmosphere is very unlikely to occur.

It is known [31] that the sensing mechanism is strongly related to the operating temperature and accordingly to the surface reactions which take place between the CO test gas and adsorbed oxygen species. Therefore, prior to CO interaction with NiO-sensitive materials, one should admit the following interaction (Equation (2)) which takes place between atmospheric oxygen O₂ and the NiO surface adsorption site:



where e[−] is an electron from the valence band, giving rise to an accumulation layer of holes nearby the surface.

When negatively charged oxygen interacts with CO, the previously trapped electrons are returned to the valence band, healing the holes and decreasing their concentration from the accumulation region. From the electrical point of view, this translates into a variation of resistance. On the other hand, for operando conditions, besides the oxygen content, the air also has variable humidity. This can be another potential partner for CO, but it can also create surface dipoles that determine electronic affinity variations, undetectable in the electrical resistance measurement. Therefore, simultaneous electrical resistance (R) and contact potential differences (CPD) allow decoupling the physisorption from the ionosorption processes and evaluation of the electronic affinity changes (Δχ) with respect to the surrounding test gas conditions (Equation (3)).

$$q\Delta\text{CPD} = \Delta\Phi = \Phi_{\text{gas}} - \Phi_{\text{air}} = 2k_{\text{B}}T\ln(R_{\text{gas}}/R_{\text{air}}) + \Delta\chi = q\Delta V_{\text{s}} + \Delta\chi \quad (3)$$

whereby: q is the electric charge, ΔΦ is the relative work function change, Φ_{gas} is the relative work function recorded under the presence of CO; Φ_{air} is the relative work function corresponding to the reference atmosphere (e.g., 50% RH); k_B is the Boltzmann constant; T is the absolute temperature; R_{gas} is the electrical resistance under CO exposure; R_{air} is the electrical resistance under reference atmosphere; Δχ is the electron affinity change; ΔV_s is the surface potential change; and qΔV_s represents the surface band bending height.

The operation of the Kelvin probe is based on the principle of the vibrating capacitor and allows the measurement of the CPD between the NiO surface and the vibrating head of the Probe. The work function is an extremely sensitive indicator of the surface condition and is affected by the surface adsorption/desorption processes [32]. Considering the electrochemical potential of the bulk as constant, the relative work function changes due to the gas exposure are caused either by the changes in the surface potential and/or changes in the electron affinity. Only the former has an impact on the overall electrical resistance variations, whereas the latter is attributed to changes in the coverage with dipoles oriented perpendicular to the surface [33]. Well known as a polar molecule, atmospheric humidity is responsible for creating dipoles on the NiO surface. Any subsequent interaction between CO and water results in a change in electron affinity [34], according to Equation (4):

$$\Delta\chi = \Delta\Phi - q\Delta V_{\text{s}} \quad (4)$$

As such, findings about chemical species which may carry net charges (directly involved in the overall conduction mechanism) are evaluated with respect to the dipolar character of water, which is permanently present under in-field conditions.

By examining quantitatively each energetic contribution from Figures 7 and 8 and the associated cartoon (Figure 9a,b), one can summarise the following results:

1. In the case of NiO1 400 ΔΦ, qΔV_s and Δχ decrease with increasing CO concentration. Thus, it is plausible to assume that the reaction mechanism of CO interaction with the sensitive surface can be described by a twofold scenario: the decrease in the surface band bending is in line with the interaction between CO and pre-adsorbed oxygen species (Figure 7a), whereas the interaction with the surface hydroxyl groups is reflected by the decrease in the electronic affinity (Figure 9b). The monotonous

decrease in all three contributions indicates that the saturation in the reaction partners was not attained [35].

- In the case of NiO2 400, one can see that while $\Delta\Phi$, $q\Delta V_s$ decrease slightly through the whole range of CO concentration, the electronic affinity is constant within the measurement error. Such behaviour can be explained by associating the CO interaction only with the pre-adsorbed oxygen species and not with the surface OH groups (Figure 9a).

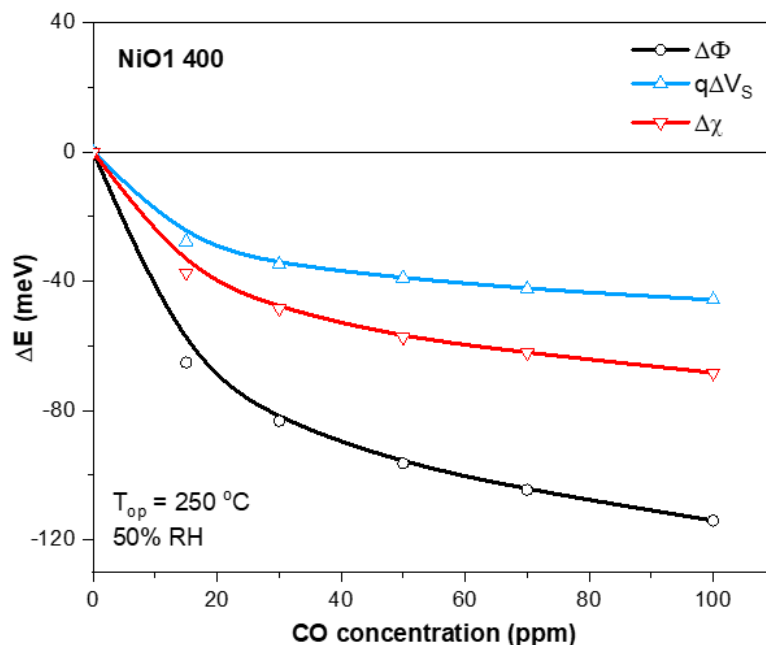


Figure 7. The decoupled energetic contributions with respect to CO concentration for NiO1 400 when operated at 250 °C under 50% RH background atmosphere.

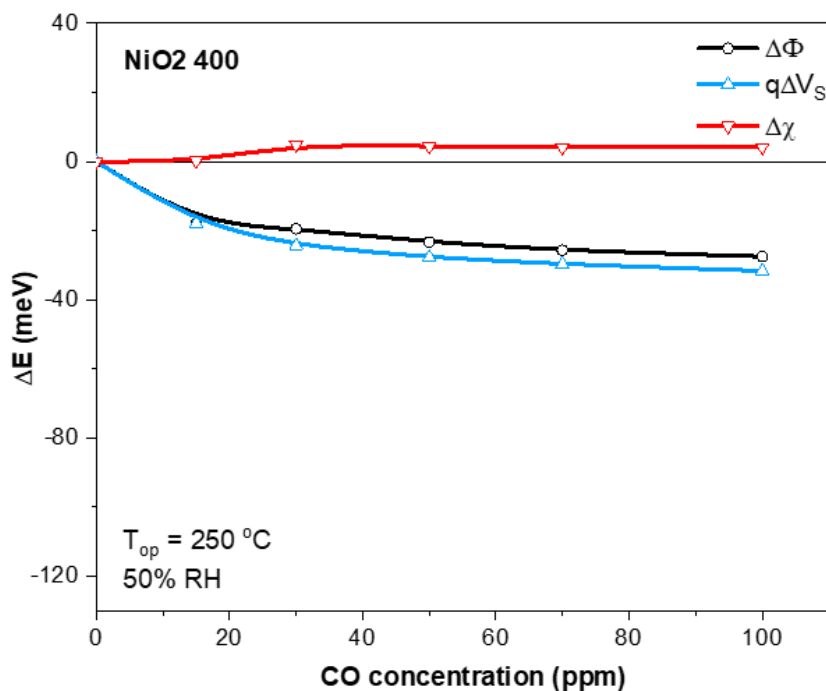


Figure 8. The decoupled energetic contributions with respect to CO concentration for NiO2 400 when operated at 250 °C under 50% RH background atmosphere.

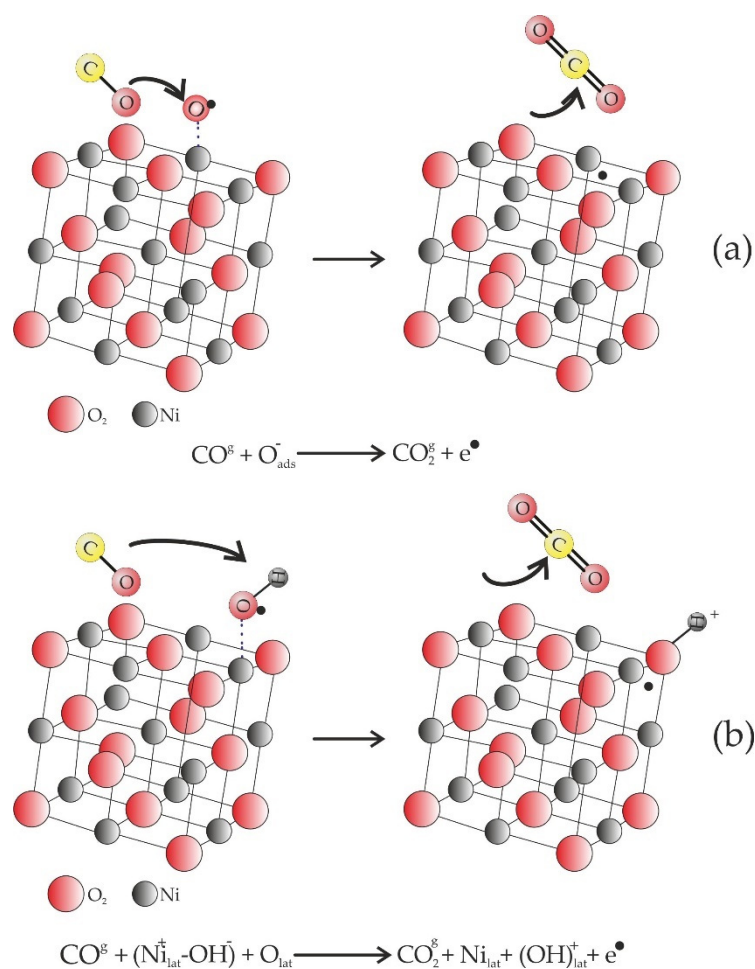


Figure 9. The associated cartoon describing the gas sensing mechanisms of both NiO1- and NiO2-based gas sensors when interacting CO with pre-adsorbed oxygen (a) and with surface hydroxyl groups (b).

Thus, one should keep in mind that different preparation strategies undertook variations within the gas–surface interaction pathways clearly highlighted by the phenomenological investigations.

By a combination of preparation parameters with extensive material characterization, a correlation between the synthesis route and material sensing properties was revealed. It was shown that fine-tuning the gas–surface reaction mechanism was possible. Accordingly, it is possible to assume that the reactions summarized in Figure 9 determine changes in the sensor response of both sensitive NiO materials. Thus, in the case of NiO1 400, the CO sensing occurs via two pathways: reaction with the pre-adsorbed oxygen species, which reduces the net surface charge trapped on the surface states, and with the surface hydroxyl groups. The latter combines with the lattice oxygen and provides donors (e.g., lattice hydroxyl groups), i.e., additional free charge carriers involved in CO detection. In the case of NiO2 400 the only interaction is with the pre-adsorbed oxygen species, a fact mirrored by a smaller sensor response in comparison with NiO1 400.

4. Conclusions

Herein, we have investigated the role induced by the different chemical synthesis routes over the CO detection mechanism with NiO-based gas sensors. The structural and morphological investigations revealed considerable differences in shape and size between the as-prepared materials. Such aspects have been correlated to the sensor responses towards different CO concentrations exposed under 10, 30 and 50% RH. In order to obtain

insights about the sensing mechanism, simultaneous electrical resistance and contact potential differences were involved. Consequently, two different interaction mechanisms have been proposed to explain the slight enhancement and downgrading in CO detection in the presence of relative humidity. The increase in the sensor response for the sensor labelled as NiO1 400 was explained via interaction between CO and both surface pre-adsorbed oxygen species and hydroxyl groups. This leads to a decrease in the surface band bending and electronic affinity, as well. The slight lowering of the sensor response for the NiO2 400 was explained by a onefold CO interaction mechanism solely with the pre-adsorbed oxygen. This was mirrored by the decrease in band bending while keeping the electronic affinity constant.

Author Contributions: Conceptualization, C.E.S. and A.S.; XRD investigations, D.G.; TEM investigations, C.G., C.G.M. and D.G.; writing—original draft preparation, C.E.S.; writing—review and editing, all authors. All authors have read and agreed to the published version of the manuscript.

Funding: This work was supported by the Ministry of Research, Innovation and Digitization CNCS-UEFISCDI through the projects PN-III-P4-ID-PCE-2020-0506 and PN-III-P4-PCE-2021-0384 within PNCDI III and by the Romanian National Authority for Scientific Research through the Core Program PN19-03 (contract No. 21 N/08.02.2019). The contribution of Catalina G. Mihalcea (C.G.M.) to this work is part of the PhD “Nanostructured materials for gas sensing: correlations between functional, electronic and microstructural properties” supported by CERIC-ERIC.

Institutional Review Board Statement: Not applicable.

Informed Consent Statement: Not applicable.

Data Availability Statement: Not applicable.

Acknowledgments: C.E.S thank S. Somacescu for preparing the NiO materials and to Eng. O.G. Florea for sensors fabrication.

Conflicts of Interest: The authors declare no conflict of interest.

References

1. Brattain, W.H.; Bardeen, J. Surface Properties of Germanium. *Bell Syst. Tech. J.* **1953**, *32*, 1–41. [[CrossRef](#)]
2. Taguchi, N. Gas Alarm Devices. Patent JPB_1970038200, 1962.
3. Dhall, S.; Mehta, B.R.; Tyagi, A.K.; Sood, K. A review on environmental gas sensors: Materials and technologies. *Sens. Int.* **2021**, *2*, 100116. [[CrossRef](#)]
4. Staerz, A.; Weimar, U.; Barsan, N. Current state of knowledge on the metal oxide based gas sensing mechanism. *Sens. Actuators B Chem.* **2022**, *358*, 131531. [[CrossRef](#)]
5. Staerz, A.; Bahri, M.; Geyik, U.; Brinkmann, H.; Weimar, U.; Ersen, O.; Barsan, N. Direct Microscopic Proof of the Fermi Level Pinning Gas-Sensing Mechanism: The case of Platinum-Loaded WO₃. *J. Phys. Chem. Lett.* **2020**, *11*, 166–171. [[CrossRef](#)]
6. Kim, D.S.; Lee, H.C. Nickel vacancy behavior in the electrical conductance of nonstoichiometric nickel oxide film. *J. Appl. Phys.* **2012**, *112*, 034504. [[CrossRef](#)]
7. Gao, X.; Lin, W.; Ge, Z.; Ge, H.; Kawi, S. Modification Strategies of Ni-Based Catalysts with Metal Oxides for Dry Reforming of Methane. *Methane* **2022**, *1*, 139–157. [[CrossRef](#)]
8. Xu, X.; Zhang, H.; Tong, Y.; Sun, Y.; Fang, X.; Xu, J.; Wang, X. Tuning Ni³⁺ quantity of NiO via doping of cations with varied valence states: The key role of Ni³⁺ on reactivity. *Appl. Surf. Sci.* **2021**, *550*, 149316. [[CrossRef](#)]
9. Raza, M.H.; Movlaee, K.; Leonardi, S.G.; Barsan, N.; Meri, G.; Pinna, N. Gas sensing of NiO-SCCNT Core-Shell Heterostructures: Optimization by Radial Modulation of the Hole-Accumulation. Layer. *Adv. Funct. Mat.* **2020**, *30*, 1906874. [[CrossRef](#)]
10. Barsan, N.; Simion, C.; Heine, T.; Pokhrel, S.; Weimar, U. Modeling of sensing and transduction for p-type semiconducting metal oxide based gas sensors. *J. Electroceramics* **2010**, *20*, 11–19. [[CrossRef](#)]
11. Stanoiu, A.; Ghica, C.; Mihalcea, C.G.; Ghica, D.; Somacescu, S.; Florea, O.G.; Simion, C.E. Effects of Calcination Temperature on CO-Sensing Mechanism for NiO-Based Gas Sensors. *Chemosensors* **2022**, *10*, 191. [[CrossRef](#)]
12. Ayyala, S.K.; Covington, J.A. Nickel-Oxide Based Thick-Film Gas Sensors for Volatile Organic Compound Detection. *Chemosensors* **2021**, *9*, 247. [[CrossRef](#)]
13. Prajesh, R.; Goyal, V.; Nahid, M.; Saini, V.; Singh, A.K.; Sharma, A.K.; Bhargava, J.; Agarwal, A. Nickel oxide (NiO) thin film optimization by reactive sputtering for highly sensitive formaldehyde sensing. *Sens. Actuators B Chem.* **2020**, *318*, 128166. [[CrossRef](#)]

14. Mokoena, T.P.; Hillie, K.T.; Swart, H.C.; Leshabane, N.; Tshilongo, J.; Motaung, D.E. Fabrication of a propanol gas sensor using p-type nickel oxide nanostructures: The effect of ramping rate towards luminescence and gas sensing characteristics. *Mater. Chem. Phys.* **2020**, *253*, 123316. [[CrossRef](#)]
15. Qian, G.; Peng, Q.; Zou, D.; Wang, S.; Yan, B. Hydrothermal Synthesis of Flake-Flower NiO and Its Gas Sensing Performance to CO. *Front. Mater.* **2020**, *7*, 216. [[CrossRef](#)]
16. Simion, C.E.; Ghica, C.; Mihalcea, C.G.; Ghica, D.; Mercioniu, I.; Somacescu, S.; Florea, O.G.; Stanoiu, A. Insights about CO Gas-Sensing Mechanism with NiO-Based Gas Sensors—The Influence of Humidity. *Chemosensors* **2021**, *9*, 244. [[CrossRef](#)]
17. Ghica, C.; Mihalcea, C.G.; Simion, C.E.; Vlaicu, I.D.; Chica, D.; Dinu, I.V.; Florea, O.G.; Stanoiu, A. Influence of relative humidity on CO₂ interaction mechanism for Gd-doped SnO₂ with respect to pure SnO₂ and Gd₂O₃. *Sens. Actuators B Chem.* **2022**, *368*, 132130. [[CrossRef](#)]
18. Yamazoe, N.; Shimano, K. Roles of Shape and Size of Component Crystals in Semiconductor Gas Sensors: I. Response to Oxygen. *J. Electrochem. Soc.* **2008**, *155*, J85. [[CrossRef](#)]
19. Poulain, R.; Lumbeeck, G.; Hunka, J.; Proost, J.; Savolainen, H.; Idrissi, H.; Schryvers, D.; Gauquelin, N.; Klein, A. Electronic and Chemical Properties of Nickel Oxide Thin Films and the Intrinsic Defects Compensation Mechanism. *ACS Appl. Electron. Mater.* **2022**, *4*, 2718–2728. [[CrossRef](#)]
20. Priya, M.J.; Subha, P.P.; Jayaraj, M.K. Chapter 1—Facet-dependent gas sensing properties of metal oxide nanostructures. In *Nanomaterials for Sensing and Optoelectronic Applications—Micro and Nano Technologies*; Jayaraj, M.K., Subha, P.P., Thomas, S., Eds.; Elsevier: Amsterdam, The Netherlands, 2022; pp. 1–25. [[CrossRef](#)]
21. Korotcenkov, G.; Golovanov, V.; Brinzari, V.; Cornet, A.; Morante, J.; Ivanov, M. Distinguishing feature of metal oxide films' structural engineering for gas sensor applications. *J. Phys. Conf. Ser.* **2005**, *15*, 256–261. [[CrossRef](#)]
22. Springhorn, C.; Schmalzried, H. The electronic conduction mechanism of NiO-crystals. *Ber. Der Bunsenges. Für Phys. Chem.* **1994**, *98*, 746–748. [[CrossRef](#)]
23. Karsthof, R.; Grundmann, M. Polaronic interacceptor hopping transport in intrinsically doped nickel oxide. *Phys. Rev. B* **2019**, *99*, 235201. [[CrossRef](#)]
24. Hahn, S.H.; Bãrsan, N.; Weimar, U.; Ejakov, S.G.; Visser, J.H.; Soltis, R.E. CO sensing with SnO₂ thick film sensors: Role of oxygen and water vapour. *Thin Solid Films* **2003**, *436*, 17–24. [[CrossRef](#)]
25. Wicker, S.; Guiltat, M.; Weimar, U.; Hemeryck, A.; Bãrsan, N. Ambient Humidity Influence on CO Detection with SnO₂ Gas Sensing Materials—A Combined DRIFTS/DFT Investigation. *J. Phys. Chem. C* **2017**, *121*, 25064–25073. [[CrossRef](#)]
26. Clifford, P.K.; Tuma, D.T. Characteristics of semiconductor gas sensors I. Steady state gas response. *Sens. Actuators B Chem.* **1982**, *3*, 233–254. [[CrossRef](#)]
27. Yamazoe, N.; Shimano, K. Theory of power laws for semiconductor gas sensors. *Sens. Actuators B Chem.* **2008**, *128*, 566–573. [[CrossRef](#)]
28. Sasi, B.; Gopchandran, K.G. Nanostructured mesoporous nickel oxide thin films. *Nanotechnology* **2007**, *18*, 115613. [[CrossRef](#)]
29. Sawatzky, G.A.; Allen, J.W. Magnitude and Origin of the Band-Gap in NiO. *Phys. Rev. Lett.* **1984**, *53*, 2339–2342. [[CrossRef](#)]
30. Cho, D.-Y.; Song, S.J.; Kim, U.K.; Kim, K.M.; Lee, H.-K.; Hwang, C.S. Spectroscopic investigation of the hole states in Ni-deficient NiO films. *J. Mater. Chem. C* **2013**, *1*, 4334–4338. [[CrossRef](#)]
31. Sharma, A.; Rout, C.S. Advances in understanding the gas sensing mechanisms by in situ and operando spectroscopy. *J. Mat. Chem. A* **2021**, *9*, 18175–18207. [[CrossRef](#)]
32. Oprea, A.; Bãrsan, N.; Weimar, U. Work function changes in gas sensitive materials: Fundamentals and applications. *Sens. Actuators B Chem.* **2009**, *142*, 470–493. [[CrossRef](#)]
33. Khan, A. Fermi level, work function and vacuum level. *Mater. Horiz.* **2016**, *3*, 7–10. [[CrossRef](#)]
34. Koziej, D.; Bãrsan, N.; Weimar, U.; Szuber, J.; Shimano, K.; Yamazoe, N. Water-oxygen interplay on tin dioxide surface: Implication on gas sensing. *Chem. Phys. Lett.* **2005**, *410*, 321–323. [[CrossRef](#)]
35. Li, S.; Zhang, M.; Wang, H. Simulation of gas sensing mechanism of porous metal oxide semiconductor sensor based on finite element analysis. *Sci. Rep.* **2021**, *11*, 17158. [[CrossRef](#)] [[PubMed](#)]